Projection phase contrast microscopy with a hard x-ray nanofocused beam: Defocus and contrast transfer

T. Salditt,[1] K. Giewekemeyer,[1] C. Fuhse,[1] S. P. Krüger,[1] R. Tucoulou,[2] and P. Cloetens[2]
[1]*Institut für Röntgenphysik, Universität Göttingen, Friedrich-Hund-Platz 1, 37077 Göttingen, Germany*
[2]*ESRF, BP 220, 38043 Grenoble, France*
(Received 14 December 2008; published 29 May 2009)

We report a projection phase contrast microscopy experiment using hard x-ray pink beam undulator radiation focused by an adaptive mirror system to 100–200 nm spot size. This source is used to illuminate a lithographic test pattern with a well-controlled range of spatial frequencies. The oscillatory nature of the contrast transfer function with source-to-sample distance in this holographic imaging scheme is quantified and the validity of the weak phase object approximation is confirmed for the experimental conditions.

DOI: 10.1103/PhysRevB.79.184112 PACS number(s): 07.85.Tt, 42.30.Lr, 42.40.−i, 68.37.Yz

I. INTRODUCTION

Holographic x-ray projection microscopy, based on the principle of holography,[1] projection magnification,[2] and Fresnel imaging,[3,4] yields quantitative images of hard and soft materials in electron density[5] or magnetization[6] contrast at the nanoscale. An extension from two-dimensional (2D) projection images to three-dimensional (3D) data sets by holographic tomography is relatively straightforward. By definition, holography makes use of the interference terms $2\,\mathrm{Re}[\psi_s\psi_o^*]$ between a scattered wave ψ_s and a reference wave ψ_o. Hence a weak scattered signal can be amplified high above background signals of residual scatter, presenting a dose-efficient alternative to coherent diffractive imaging (CDI), which uses the far-field diffraction pattern $\psi_s\psi_s^*$ as input.[7–12] Furthermore, holographic image reconstruction is a deterministic one-step process, in contrast to the iterative image reconstruction in CDI algorithms,[7,10] where central issues of uniqueness, convergence, reconstruction speed, as well as optimum choice of initial phases are yet unsolved in a strict mathematical sense.

With increasing resolution and photon energy needed to penetrate bulk samples, absorption contrast becomes negligible and phase contrast prevails. The image formation of holographic (projection) microscopy based on a hard x-ray quasipoint source can be described by free-space propagation after modulation of the spherical wave front by the object.[13,14] X-ray projection microscopy has been pioneered both theoretically and experimentally by Wilkins and collaborators, who have used a scanning electron based in-house x-ray source.[14–16] As the demand for high resolution and shorter accumulation times becomes stronger, we present here an in-line holography experiment based on highly efficient and adaptive hard x-ray focusing by the Kirkpatrick-Baez mirror system[17] of the European Synchrotron Radiation Facility (ESRF, Grenoble). We use a tailored lithographic test pattern to quantitatively verify that the complex contrast transfer function (CTF) shows the predicted oscillatory behavior with the so-called defocus (source-to-sample) distance. The zeros of the CTF are detected directly by contrast reversal in the holograms of the test structure. We thus show that image formation in experimentally relevant conditions using a partially coherent full undulator harmonic can be described using the approximation of a weak phase object, and that the oscillatory nature of the CTF must be taken into account in holographic reconstruction.

II. PHASE CTF

Following Refs. 15 and 18 we briefly consider the wave optical fundamentals of the contrast transfer function in the limit of a weak phase object. From the Fresnel-Kirchhoff equation, the wave field $E_2(x_2,y_2)$ in the detector plane downstream from the object plane is determined by superposition of waves exiting from the object plane $E_1(x_1,y_1)$. After transformation to Fourier space (indicated by a tilde), this propagation reduces to a simple multiplication with the free-space propagator h_z in Fourier space $\tilde{E}_2=\tilde{h}_z\tilde{E}_1$. In the paraxial approximation, well justified for hard x-ray imaging, the propagator is given by

$$\tilde{h}_z(\nu_x,\nu_y)=\exp(ikz)\,\exp[-i\pi\lambda z(\nu_x^2+\nu_y^2)], \tag{1}$$

where ν_x and ν_y denote the respective spatial frequencies. We now consider a plane-wave illuminating a thin object located in the object plane. The (complex) optical-transmission function $\tau(x,y)$ of the object is defined by the integral of the local index of refraction $n=1-\delta+i\beta$ over the sample thickness t along the axis of propagation. The real and imaginary components of the index define the phase shift $\phi(x_1,y_1)$ and the attenuation term $\mu(x_1,y_1)$, respectively,

$$\tau(x,y)=\exp[ik(1-\langle n(x,y)\rangle_t)t] \tag{2}$$

$$=\exp[ikt]\exp[i\phi(x,y)-\mu(x,y)/2], \tag{3}$$

where $\langle\ldots\rangle_t$ denotes the average over t along the optical path. For samples which are uniform along the propagation axis z, the two terms are simply $\phi=-k\delta t\simeq\rho_e r_e t\lambda$ and $\mu=2k\beta t$. The phase shift thus reflects the local electron density projected along the thickness and the full 3D structure can be reconstructed tomographically. For weak objects where ϕ and μ are small compared to 1, τ can be expanded

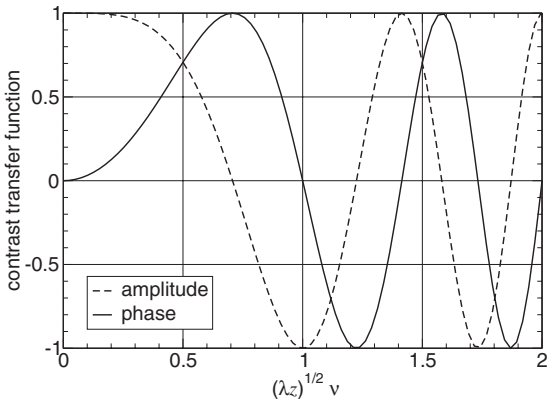

FIG. 1. Contrast transfer functions for phase and amplitude objects as a function of the normalized spatial frequency $\sqrt{\lambda z}\nu$.

$$\tau(x,y) = \exp[i\phi(x,y) - \mu(x,y)/2] \approx 1 + i\phi(x,y) - \mu(x,y)/2. \tag{4}$$

Applying Eq. (1), we find for the wave field in plane S_2 further downstream in Fourier space

$$\tilde{E}_2(\nu_x,\nu_y) = \tilde{\tau}\tilde{h}_z \simeq [\delta_D(\nu_x,\nu_y) + i\tilde{\phi}(\nu_x,\nu_y) - \tilde{\mu}(\nu_x,\nu_y)/2] \times \exp(ikz)\exp[-i\pi\lambda z(\nu_x^2+\nu_y^2)], \tag{5}$$

where δ_D denotes the Dirac delta function representing the directly transmitted beam. To first order in ϕ and μ the corresponding intensity $I=|E_2|^2$ is given in Fourier space by[15]

$$\tilde{I}(\nu_x,\nu_y) \approx \delta_D(\nu_x,\nu_y) + 2\tilde{\phi}(\nu_x,\nu_y)\sin\chi - \tilde{\mu}(\nu_x,\nu_y)\cos\chi, \tag{6}$$

with $\chi=\pi\lambda z(\nu_x^2+\nu_y^2)$. $\sin\chi$ and $\cos\chi$ in this equation are termed the phase and amplitude CTFs and are plotted in Fig. 1 as a function of the spatial frequency ν. Thus, the CTF acts as a linear filter to the object transmission function. Directly behind the object ($z=0$), the intensity distribution shows pure and maximum amplitude contrast and phase contrast is zero. With increasing z, amplitude contrast decreases and phase contrast increases, as long as $\chi \leq \pi/2$. At spatial frequencies and defocus distances, for which the approximation $\sin\chi \approx \chi$ holds, the intensity behind a pure phase object is given by[15]

$$\tilde{I}(\nu_x,\nu_y) = \delta_D(u,v) + 2\pi\lambda z(\nu_x^2+\nu_y^2)\tilde{\phi}(\nu_x,\nu_y). \tag{7}$$

Accordingly, intensity in real space is proportional to the two-dimensional Laplacian $\nabla_\perp^2$ of the phase shift and to the distance z

$$I(x,y) = 1 - \frac{\lambda z}{2\pi}\nabla_\perp^2\phi(x,y). \tag{8}$$

This equation, valid under the above assumption $\sin\chi \approx \chi$, shows that in this imaging regime the x-ray wavelength is a simple prefactor which determines the magnitude of the intensity variations. Note, that since $\phi \propto \lambda$, the prefactor is proportional to λ^2, when the intensity contrast is written in terms of electron density rather than phase shift. High monochromaticity is not required in this regime and a broad bandwidth may be used. With further increase in z, the absolute value as well as the sign of the image contrast varies rapidly with the spatial frequency and the x-ray wavelength, and comparably high monochromaticity is required. Since the image of an object typically contains a range of spatial frequencies, large features (corresponding to small spatial frequencies) may be in the direct-contrast regime, while small features (corresponding to high spatial frequencies) are already in the holographic regime.

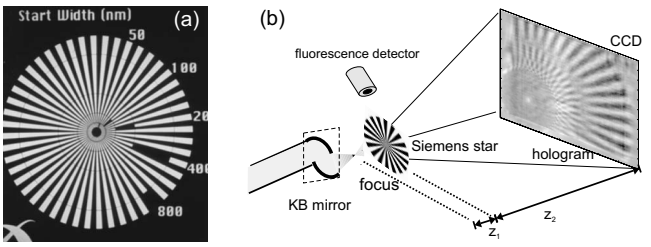

FIG. 2. (a) Micrograph of the lithographic test sample. (b) Setup of in-line holography.

A well-defined test structure with controlled increase in spatial frequencies from the outer to the inner regions is given by the well-known *Siemens star* design, see Fig. 2. Let us now turn to the projection geometry used here. The parallel beam propagation considered above can be mapped to a projection geometry of a divergent beam emitted from a point source.[15,19] Given a distance z_1 between source and sample and z_2 between sample and detector, the same formalism as above can be applied if after a simple variable transformation (for the detailed calculation see Ref. 19), with the effective defocus (propagation) distance given by $z = z_1 z_2/(z_1+z_2)$. At the same time the hologram is magnified corresponding to the geometrical projection by a factor of $M=(z_1+z_2)/z_1$.

III. EXPERIMENT

The experiment was performed at the ID22NI undulator beamline at the third generation synchrotron facility ESRF, Grenoble. Two undulators were used simultaneously working at the second and fifth harmonic, respectively. The radiation was used in the so-called pink mode (no crystal monochromators) at a photon energy of $E=17.5$ keV, using the intrinsic monochromaticity of the undulators and the bandpass of the multilayer Kirkpatrick-Baez (KB) mirror system resulting in about $\Delta\lambda/\lambda \simeq 0.02$. In addition, a flat horizontally deflecting Pd-coated Si mirror was used at 0.15° incidence angle for higher harmonics rejection. The focus of the KB mirrors was characterized by translation of a Au stripe on the test pattern, recording both the transmitted intensity by a diode and the Au L_α fluorescence by a silicon drift detector (Vortex-EX, SII NanoTechnology Inc.). The measured focal spot size was $D_{\text{horz}}=160$ nm [full width at half maximum (FWHM)] in the vertical and $D_{\text{vert}}=146$ nm (FWHM) in the horizontal direction, respectively. This high demagnification of the source was possible by closing the high power slits located at about 36 m upstream from the end station horizontally to create a virtual source of 10 μm. The total intensity

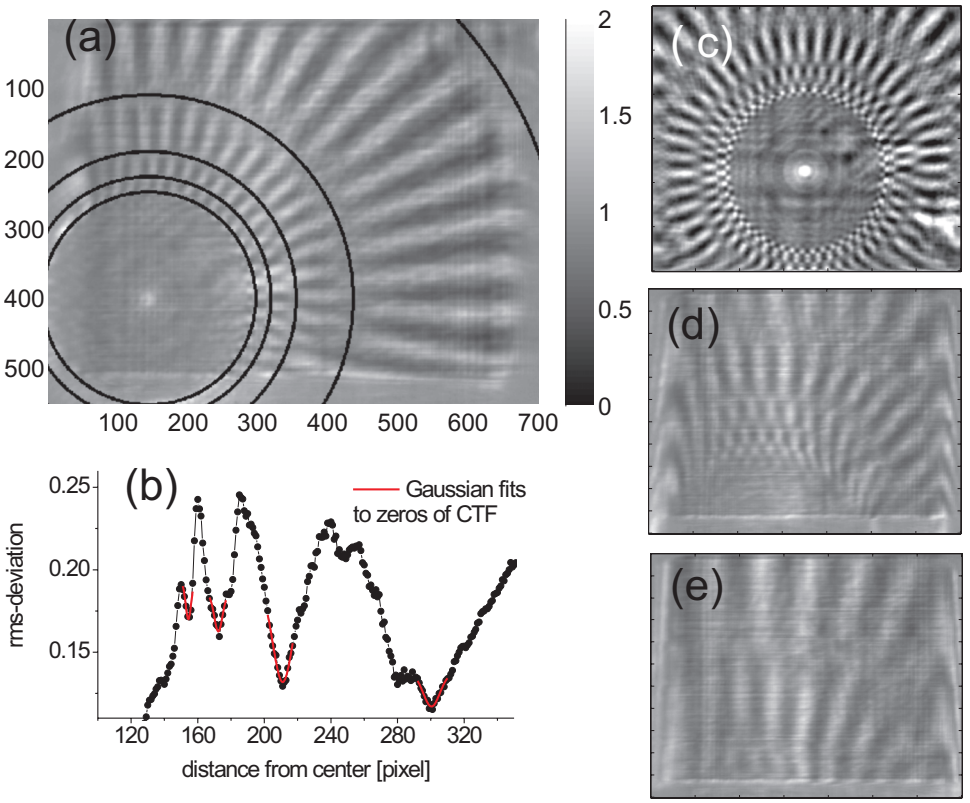

FIG. 3. (Color) (a) Hologram (projection image) recorded at $z_1=15$ mm after division by the empty beam. Circles indicate the radii where the CTF is zero. (b) The position of the circles was determined from evaluating the rms deviation of the intensity values from the mean for each pixel radius from the center. The cusps indicate the positions of the circles. The source-to-sample distance z_1 is then scanned, changing field of view and the positions of the CTF minima. For illustration, holograms recorded at (c) $z_1=15$ mm (star centered), (d) $z_1=5$ mm, and (e) $z_1=3$ mm are shown to illustrate the effect of varied defocus z. The images were divided by the empty beam. Grey scale is scales in the interval [0,2] for (a), (d), and (e) and [0.7,1.3] for (c).

in the focal spot was on the order of 10^{11} cps, depending on the ring current and the slit settings in front of the KB. A lithographic Au pattern was used as a test object (Siemens star) with a structure height of 180 nm, outer radius $R=15$ μm, and finest feature size of 50 nm, deposited on a 100–120-nm-thick Si_3N_4 membrane (calibration pattern X50–30–2m, X-radia Inc., California). At the photon energy of $E=17.5$ keV the transmission of the 180 nm Au structure is 0.963 corresponding to $\mu/2\simeq 0.019$, and the phase shift is $\phi=0.164$. Therefore the test structure is essentially a pure phase object at the experimental energy. A fast readout low-noise charge coupled device detector (FReLoN, ESRF) was used to image the in-line hologram at a distance z_2 from the sample, which in turn was positioned at varied distance z_1 behind the KB focus. The FreLoN camera records the scintillation light emitted from a scintillator foil after passing a magnifying optical system resulting in an effective pixel size of 0.96 μm.

Figure 3 shows a hologram of the Siemens star recorded at a distance $z_1=15$ mm (nominal value) and $z_2=538$ mm. The characteristic pattern consists of radial stripes intersected by rings on which the radial modulation of intensity is suppressed. These rings correspond to the spatial frequencies of zero contrast transfer, which shift systematically with z_1 or correspondingly with the so-called defocus distance z, see Figs. 3(c)–3(e). Along a radial line the contrast is inverted as the rings are crossed, in line with the predicted oscillatory nature of the CTF, see Fig. 1. The minima positions of the CTF were determined in a semiautomated manner by plotting the rms deviation of intensity $I_\sigma(R)=(\langle I^2\rangle-\langle I\rangle^2)^{0.5}$, averaged for each R over the polar angle, as a function of R, see Fig. 3(b). In many holograms, the center position (X_c,Y_c) of the Siemens star was first determined visually, followed by an iterative procedure of determining $I_\sigma(R)$ for several possible center coordinates to identify the strongest modulation in I_σ.

The spatial frequencies ν_n of zero contrast transfer correspond to the inverse periodicity (lines and spaces) for the given radius. They were calculated according to $\nu_n=r_n/(R48)$ for each hologram from the pixel values of the radii r_n, given the radius R of the star and the number of stripes $N_s=48$. Figure 4 shows the relative increase of the first-order spatial frequency ν_1 for the defocusing series normalized to the value of the reference position $z_1=15$ at the beginning of the scan. The inset shows the sequence of orders for constant $z_1=15$ mm. Both dependencies confirm the predicted relation $\nu_n=\sqrt{n/(\lambda z)}$. Absolute values of ν_n can be determined for $z_1=15$ mm, where the rim of the star is discernible in the hologram and also agree within errors. Along with the data points of the defocusing series, the function $\sqrt{z_{\max}/z}$ is plotted (solid line) with $z_{\max}=15$ mm the largest defocus distance of the image series. The defocus is calcu-

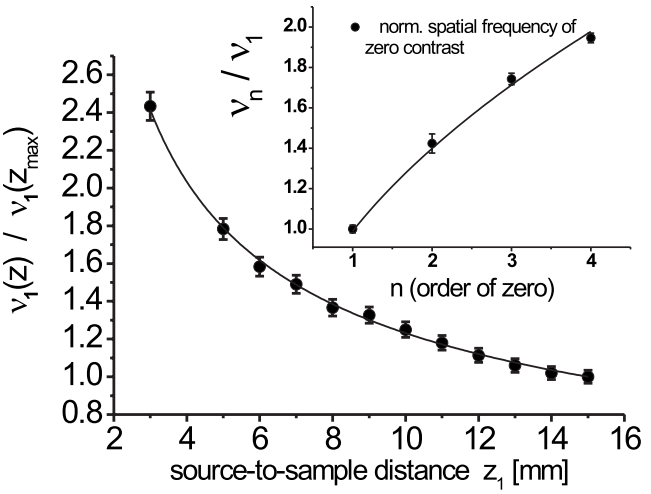

FIG. 4. Spatial frequency of zero contrast for the first order obtained from the radii in the holograms where the contrast undergoes an inversion, normalized to the position at the start of the scan along with the predicted curve $z^{-0.5}$. The insert shows the $\sqrt{n}$ scaling of the first four orders determined from Fig. 3.

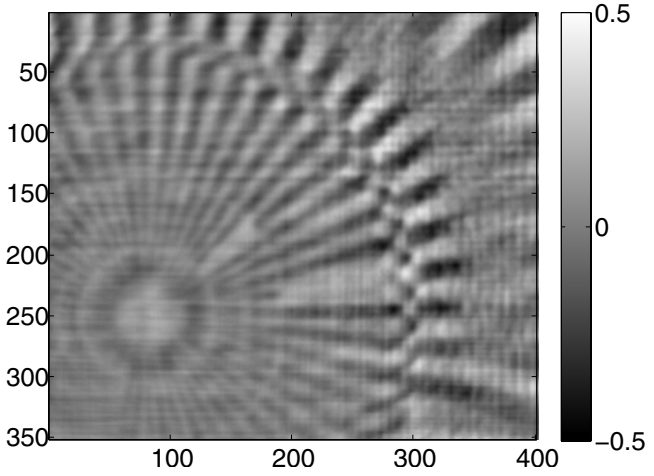

FIG. 5. One-step holographic reconstruction by Fresnel-Kirchhoff back propagation of the hologram shown Fig. 3. By identification of the void stripes in the center with the lithographic design (see Fig. 2), one recognizes contrast transfer down to about 200–100 nm, as expected. However, reconstruction from one hologram alone introduces artifacts at those spatial frequencies which are not transferred; see the blurred outer rings.

lated according to $z=z_1z_2/(z_1+z_2)$ after allowing for an offset (z_1-z_0) in the nominal and the true focus position. The one parameter fit yields $z_0=0.59$ mm and a least-squares deviation of $\chi^2=0.16$ indicating that the errors from the rms analysis have actually been overestimated. The offset of the focus with respect to the nominal value was later confirmed by holographic reconstruction (see below). A fit to the different orders (insert) according to an^b yields an exponent of $b=0.48\pm0.02$ with $\chi^2=1.08$, while a fixed exponent $b=0.5$ is almost equally well supported ($\chi^2=1.16$).

IV. RESULTS AND CONCLUSIONS

A. Implications for holographic reconstruction

Which implications does the oscillatory CTF have for holographic reconstruction? Obviously the spatial frequencies, for which the CTF is zero, are not properly transmitted and the reconstruction will lack the corresponding Fourier components. Figure 5 illustrates this point by showing a one-step holographic reconstruction by Fresnel-Kirchhoff back propagation of the hologram shown Fig. 3. The corresponding rings in real space show blurring and/or artifacts. Reconstruction from several well-chosen defocus distances is a remedy well known from parallel beam phase-contrast imaging.[20] Instead of moving the sample, the use of two detectors, e.g., one based on a semitransparent scintillator foil would allow to record two defocus distances simultaneously.[21] The fact that the focus is not a true point focus and that the focusing by KB mirrors and relatively wide opened slits in front of the KB is not coherent does not lead to any observable distortions on the spatial length scales larger than the focal diameter. To improve the resolution by an order of magnitude, coherent filtering by placing x-ray waveguides in the focal position of the KB is a promising yet technically challenging approach.[5] Note that KB focusing and x-ray waveguide optics are both essentially nondispersive, so that broad bandpass (pink beam) experiments become possible. Furthermore, coherent focusing and reconstruction schemes taking into account the phase fronts of the empty beam beyond the point source approximation may lead to an increased resolution. The use of support constraints and corresponding reconstruction algorithms, which are well established in coherent diffractive imaging, can be combined with holographic reconstruction,[22] and applied to the current imaging scheme.

B. Validity of the weak phase shift approximation

The experimental results indicate that broad bandpass (pink beam) focused undulator radiation can be used for holographic imaging and that the phase shift of a multi (17.5) keV photon beam induced by a "typical" nanoscale object justifies the weak phase object approximation in the sense that the predicted and measured behavior of the CFT agrees quantitatively for the test pattern used.

Applications of this holographic method can be found to be either in the domain of solid-state physics and materials science or in the biomolecular and biomedical sciences. In the first case the validity of the weak phase approximation must be checked for each sample system while the case for imaging of biological cells and tissues can be briefly estimated here. Considering the linear absorption coefficient from the x-ray optical constants[23] and elemental composition of biological tissue,[24] one recognizes the dominant effect of C and O disregarding mineralized tissue. The absorption of the light elements can easily be interpolated for plotting convenience, and one realizes that biological tissues up to a thickness of $t=1$ mm absorb less than 10% at 17.5 keV. Neglecting absorption in image formation is even better justified, since the density variations of internal structures to be resolved are expected to be smaller than the average density.

From the contrast between water and protein, a value around 10% seems reasonable. Likewise, for hydrated or embedded samples, only the internal density variations with respect to the average (water) density are important for image formation. If these amplitudes are again estimated to be 10% of the water density, the phase shift of 50 μm tissue is about 0.1π for 17.5 keV. Thus, reasonable biological samples for nanoscale imaging are essentially always phase objects at the given energy, but not always weak phase objects. However, for studies of thin slices and single cells, the weak phase object approximation is very well justified.

C. Coherence requirements

Finally, we consider the affordable bandpass and coherence for such experiments. Assuming for the sake of simplicity a Gaussian near-field distribution in the focal plane $z=0$ given by $I/I_0=\exp(-r^2/2r_0^2)$, with a $(1/\sqrt{e})$-radius r_0, or equivalently $D=2r_0$ the source diameter. Following from the well-known Gaussian beam propagation formula[25] the intensity distribution at z_1 has a waist $r(z_1)=r_0\sqrt{1+(\lambda z_1)^2/(4\pi r_0^2)^2}$. In the far field $z_1 \gg 4\pi r_0^2/\lambda$, the beam divergence $(1/\sqrt{e})$ half angle is $\theta=\lambda/(4\pi r_0)$. Thus the full beam diameter $L=2\theta z_1$ is equal to the spatial coherence length $\xi_\perp=\lambda z_1/(\pi D)$, for a source of diameter D (and arbitrary coherence properties), observed at a distance z_1.[25] In other words, as expected for a diffraction limited beam, the diffracted beam is fully coherent for any practical $z_1 \gg 4\pi r_0^2/\lambda$, which is not a restrictive condition for projection propagation imaging, even if the focusing scheme itself is not fully coherent (as is the case here).

The spectral bandpass, which determines the longitudinal coherence $\xi_\parallel \simeq \lambda^2/\Delta\lambda$, is another issue. In Eq. (8), we already saw that λz enters as a prefactor in the regime $\sin\chi \simeq \chi$, thus for small defocus $z_1 \ll [\pi\lambda_1(\nu_x^2+\nu_y^2)]^{-1}$. Here, high bandpass can be tolerated without spoiling the image. However, the corresponding small value of z_1 also implies small beam diameter at the sample $L=2\theta z_1=\lambda z_1/(\pi D)$, and hence small field of view. As z_1 is increased, the oscillatory nature of CTF comes into effect with a decreasing spacing between minima and maxima. According to Eq. (1), the two ends of a wavelength interval $\Delta\lambda$ will fall onto a maximum and a minimum of the CTF, respectively, if $\Delta\lambda=[z_1(\nu_x^2+\nu_y^2)]^{-1}$, thus cancelling the contrast. Therefore the bandpass must be sufficiently small $(\Delta\lambda/\lambda) \leq [\lambda z_1(\nu_x^2+\nu_y^2)]^{-1}$, to avoid a smearing of the intensity fringes in the hologram. Expanding with πD, and using the relation for the beam size at the sample $L=\lambda z_1/(\pi D)$ in small angle approximation, we get

$$\frac{\Delta\lambda}{\lambda} \leq \frac{1}{\pi DL(\nu_x^2+\nu_y^2)^2}. \tag{9}$$

The above condition is most restrictive for the high spatial frequencies indicating a loss of resolution if the bandpass is too large. Since one should aim a resolution close to the source size D, we can demand $\nu \leq 1/D$, and hence the maximum tolerable bandpass becomes

$$\frac{\Delta\lambda}{\lambda} \leq \frac{D}{\pi L}. \tag{10}$$

The intensity optimized bandpass without compromising the resolution is thus given by the ratio between field of view and the resolution element, or stated differently, by the number of pixels in the object plane when the field of view is to be sampled at the resolution D. The prefactor π follows from the definition used above, based on the $(1/\sqrt{e})$ width of the Gaussian beam, and would of course be different for other functions and/or width definitions. Therefore, large defocus distances z_1 with correspondingly larger field of views, necessitate higher monochromaticity than small z_1. For broad bandpass, lateral raster scan at small z_1 is a suitable way to increase the effective field of view. For illustration, we have included a movie of scanning the test structure through the beam (supplemental material, online).[26]

D. Summary

In summary, we have shown that the image formation and object reconstruction using multi-keV pink beam undulator radiation can be modeled within the approximation of weak phase objects for many relevant nanoscopic samples. The oscillatory nature of the CTF itself must be taken into account in holographic and/or iterative object reconstruction. From the results presented here, we can validate the scheme of "photon-rich" broad bandpass focusing by highly efficient mirror system for quantitative holographic projection microscopy. Despite the incoherent (or partially coherent) focusing, phase contrast is obtained for length scales larger than the focal spot. With the given photon flux in the focused beam, accumulations in the millisecond range become feasible. This opens the route for fast holographic tomography, providing quantitative bulk (3D) density maps of functional materials and biomolecular samples after fixation.

ACKNOWLEDGMENTS

We acknowledge ESRF for beamtime and the Deutsche Forschungsgemeinschaft for financial support through SFB755 *Nanoscale Photonic Imaging*, as well as through the Courant Research Center for Nanospectroscopy and X-ray Imaging.

[1] D. Gabor, Nature (London) **161**, 777 (1948).
[2] V. E. Cosslett and W. C. Nixon, J. Appl. Phys. **24**, 616 (1953).
[3] J. P. Guigay, Optik (Jena) **49**, 121 (1977).
[4] J. Cowley, *Diffraction Physics*, 3rd ed. (North-Holland, Amsterdam, 1995).
[5] C. Fuhse, C. Ollinger, and T. Salditt, Phys. Rev. Lett. **97**, 254801 (2006).
[6] S. Eisebitt, J. Lüning, W. F. Schlotter, M. Lörgen, O. Hellwig, W.

Eberhardt, and J. Stöhr, Nature (London) **432**, 885 (2004).
[7] J. R. Fienup, Appl. Opt. **21**, 2758 (1982).
[8] J. Miao, P. Charalambous, J. Kirz, and D. Sayre, Nature (London) **400**, 342 (1999); J. Miao, T. Ishikawa, B. Johnson, E. H. Anderson, B. Lai, and K. O. Hodgson, Phys. Rev. Lett. **89**, 088303 (2002).
[9] H. N. Chapman, A. Barty, M. J. Bogan, S. Boutet, M. Frank, S. P. Hau-Riege, S. Marchesini, B. W. Woods, S. C. Bajt, W. H. Benner, R. A. London, E. Plönjes, M. Kuhlmann, R. Treusch, S. Düsterer, T. Tschentscher, J. R. Schneider, E. Spiller, T. Möller, C. Bostedt, M. Hoener, D. A. Shapiro, K. O. Hodgson, D. van der Spoel, F. Burmeister, M. Bergh, C. Caleman, G. Huldt, M. M. Seibert, F. R. N. C. Maia, R. W. Lee, A. Szöke, N. Timneanu, and J. Hajdu, Nat. Phys. **2**, 839 (2006).
[10] S. Marchesini, Rev. Sci. Instrum. **78**, 011301 (2007).
[11] P. Thibault, M. Dierolf, A. Menzel, O. Bunk, C. David, and F. Pfeiffer, Science **321**, 379 (2008).
[12] C. G. Schroer, P. Boye, J. M. Feldkamp, J. Patommel, A. Schropp, A. Schwab, S. Stephan, M. Burghammer, S. Schöder, and C. Riekel, Phys. Rev. Lett. **101**, 090801 (2008).
[13] K. A. Nugent, Phys. Rev. Lett. **68**, 2261 (1992).
[14] S. W. Wilkins, T. E. Gureyev, D. Gao, A. Pogany, and A. W. Stevenson, Nature (London) **384**, 335 (1996).
[15] S. C. Mayo, P. R. Miller, S. W. Wilkins, T. J. Davis, D. Gao, T. E. Gureyev, D. Paganin, D. J. Parry, A. Pogany, and A. W. Stevenson, J. Microsc. **207**, 79 (2002).
[16] T. E. Gureyev, S. Mayo, S. W. Wilkins, D. Paganin, and A. W. Stevenson, Phys. Rev. Lett. **86**, 5827 (2001); T. E. Gureyev, D. M. Paganin, A. W. Stevenson, S. C. Mayo, and S. W. Wilkins, *ibid.* **93**, 068103 (2004).
[17] O. Hignette, P. Cloetens, G. Rostaing, P. Bernard, and C. Morawe, Rev. Sci. Instrum. **76**, 063709 (2005).
[18] A. Pogany, D. Gao, and S. Wilkins, Rev. Sci. Instrum. **68**, 2774 (1997).
[19] C. Fuhse, Ph.D. dissertation, Universität Göttingen, 2006.
[20] P. Cloetens, W. Ludwig, J. Baruchel, D. Van Dyck, J. Van Landuyt, J. P. Guigay, and M. Schlenker, Appl. Phys. Lett. **75**, 2912 (1999).
[21] H. Poulsen, *Three-Dimensional X-ray Diffraction Microscopy: Mapping Polycrystals and Their Dynamics*, Springer Tracts in Modern Physics Vol. 205 (Springer, New York, 2004).
[22] L. De Caro, C. Giannini, D. Pelliccia, C. Mocuta, T. H. Metzger, A. Guagliardi, A. Cedola, I. Burkeeva, and S. Lagomarsino, Phys. Rev. B **77**, 081408(R) (2008).
[23] http://physics.nist.gov/PhysRefData/XrayMassCoef
[24] Z.- M. Wang, R. N. Pierson, and S. B. Heymsfeld, Am. J. Clin. Nutr. **56**, 19 (1992).
[25] D. Attwood, *Soft X-rays and Extreme Ultraviolet Radiation: Principles and Applications* (Cambridge University Press, New York, 2000).
[26] See EPAPS Document No. E-PRBMDO-79-074918 for a movie of scanning the test structure through the beam. For more information on EPAPS, see http://www.aip.org/pubservs/epaps.html.